## Abstract

We used X-ray computed tomography (CT), microscopy and hardness measurements to study Al-Si10-Mg produced by selective laser melting (SLM). Specimens were subject to a series of heat treatments including annealing and precipitation hardening. The specimen interiors were imaged with X-ray CT, allowing the non-destructive quantification and characterisation of pores, including their spatial distribution. The specimens had porosities less than 0.1%, but included some pores with effective cross-sectional diameters up to 260 µm. The largest pores were highly anisotropic, being flat and lying in the plane normal to the build direction. Annealing cycles caused significant coarsening of the microstructure and a reduction of the hardness from (114 ± 3) HV, in the as-built state, to (45 ± 1) HV, while precipitation hardening increased this to a final hardness of (59 ± 1) HV. The pore size and shape distributions were unaffected by the heat treatments. We demonstrate the applicability of CT measurements and quantitative defect analysis for the purposes of SLM process monitoring and refinement.



**Keywords**

selective laser melting; aluminium alloy; additive manufacture; X-ray computed tomography; non-destructive testing

## Introduction

Selective laser melting (SLM), as part of the now prevalent and continually expanding range of additive manufacturing (AM) processes, offers several advantages over conventional manufacturing methods, such as casting, forging, machining, etc. These include a level of design freedom which is unconstrained by the limitations of tool accessibility[1,2]. Complex shapes, including those that stem from the use of weight saving topology optimisation[3-6] or lattice structures[7-16] can be manufactured with no additional cost or energy expenditure compared to traditional forms; in many cases the advantages of AM lie in its facility to produce shapes that are not achievable by other means. Additional benefits include low material wastage and a reduction of the number of manufacturing steps[1,2,17,18].

The properties of metal parts produced by SLM differ from conventionally manufactured parts in a number of ways. Two of the most prominent differences relate to porosity, which can reach significant levels if the SLM process parameters are not properly optimised, and microstructure, which for SLM parts is generally much finer than is conventionally achieved, due to the rapid solidification of the material from its molten state[18-24]. Porosity is associated with reduced mechanical properties such as strength and fatigue performance. This is because pores facilitate crack propagation, and this is especially true of irregular or clustered pores which provide high stress concentrations. Also, the presence of pores may lead to a reduction of the effective load-bearing cross-sectional area[25]. On the other hand, the inherently fine microstructure of SLM material has been shown to provide high levels of hardness and strength without the need for post-manufacture heat treatments[19]; depending on the particular alloy in question, the disadvantage is often relatively poor ductility[18].

The microstructure of SLM materials can be altered by heat treatments[18,26,27], but the effect of such treatments on internal pores has so far gone unexamined. This is important because the mechanical properties of parts are determined by the microstructure *and* the porosity, so the combined effect of any post-manufacture process on both of these properties must be understood if optimum mechanical properties are to be obtained. The pores may be affected by the relaxation of residual stresses (which can reach up to several hundred MPa[24,28]) and stress gradients, which are known to arise in SLM materials[24,28,29] as a result of the manufacturing process. In addition, heat treatments cause thermal expansion stresses, which can generate further stress gradients and drive vacancy movement, clustering, pore formation and pore growth[30].

Al-Si10-Mg was examined here as it is a well-established hardenable alloy, with $Mg_2Si$ particles being the main strengthening precipitate[31,32], and has received prior attention in the field of SLM[14,19,20,23]. X-ray CT has previously been employed to study porosity in Al-Si-Cu castings[33], aluminium and ceramic foams[34,35], and SLM stainless steel 316L[36], while pore quantification methods have been used by Marcu Puscas et al. [37], Pavanti et al.[38], Shen et al.[39],and Chawla and Deng[40] in their respective studies of sintered chromium steels, unalloyed iron, titanium and Fe-Mo0.85 steel. Most recently, Tammas-Williams et al.[41] used CT to examine Ti-6Al-4V made by electron beam melting (EBM), a similar process to SLM, which delivers energy to a metal powder bed via an electron beam rather than a laser. The authors considered porosity levels, as well as pore size and position, and found correlations with the scanning strategies used to manufacture their specimens.

X-ray computed tomography (CT) has been used here to measure the spatial distribution, size and shape of the pores in Al-Si10-Mg SLM parts in a series of heat treated conditions. Pore morphologies are presented alongside an examination of the SLM material's microstructure and hardness evolution over the same range of heat treatments. In addition to investigating the effect of the heat treatments

on porosity and microstructure, this work aims to highlight the ways in which X-ray CT and quantitative pore analysis can aid the SLM manufacturing and part validation process. In a high-value industrial setting, where confidence in the quality and repeatability of manufactured parts is essential, advantages may be gained by correlating the material processing conditions not just with porosity, which by CT can be accurately and reliably determined, but with the size, shape and position of pores, which play a role in determining the macroscopic mechanical properties and part performance. Obtaining this information by non-destructive means, rather than by cross-sectioning, is preferable since it reduces material wastage. Furthermore, for the purpose of porosity evaluation, two advantages offered by X-ray CT over conventional cross-sectioning and imaging are; (i) the independence of the apparent porosity on the specimen preparation procedure (i.e. grinding and polishing processes may have an impact on the size and shape of the observed pores due to metal smearing), and (ii) the facility to probe the entire three-dimensional volume of a specimen, rather than a relatively small selection of two-dimensional planes (within the constraints of specimen size and X-ray CT microscope compatibility). These advantages have the potential to significantly decrease the development time, that is the exploration of processing parameters to deliver low porosity parts, for a new material's processing by SLM.

Following this introduction we provide the details of our investigation, including methodologies for the production, heat treatment, X-ray imaging, microscopy and hardness measurements of SLM specimens. The results of the X-ray CT analysis are provided and discussed, yielding information about the evolution of SLM porosity with heat treatment. The use of quantitative X-ray CT as a tool for SLM process monitoring and control is also discussed. Lastly, we examine the specimen microstructure and hardness that result from the various heat treatments, before presenting our conclusions.

## 2. Experimental details

### 2.1 Selective laser melting

A series of Al-Si10-Mg specimens measuring (5 x 5 x 5) mm were produced using a Renishaw AM250 SLM machine. The laser power was 200 W and the powder was deposited in 25µm layers prior to each laser scan. The build platform was held at 180 $^{O}$C during part production. A meander scan pattern was used whereby the laser rastered across the parts with a hatch spacing of 80µm, a point distance of 70 µm and an exposure time of 220µs, providing an effective scanning speed of 318 mm $s^{-1}$. The direction of the hatch path of each layer was rotated by 67$^{O}$ from the previous one. Focused at the powder bed, the laser had a circular spot of diameter (68 ± 2) µm

**(Figure1)** {Al-Si10-Mg SLM specimen selected for repeated CT measurements. (a) is a photograph, while (b) shows a three-dimensional reconstruction of the specimen from CT data.}

Figure 1(a) shows one of the Al-Si10-Mg SLM specimens. The `X' was used to denote the face into which the X-ray beam would be directed during repeated CT measurements (more details are provided in section 2.3). The build direction is denoted *z*, and the top surface of each specimen, where $z$ = 5 mm, corresponds to the final layer of the SLM process. Figure 1(b) shows a three-dimensional reconstruction of the cube in 1(a), obtained from CT data.

### 2.2 Heat treatment

A specimen was selected from the series of SLM parts to be used for repeated CT measurements; these were in its as-built state and after subsequent heat treatments. Of the other specimens, one was cross-sectioned after each heat treatment to examine the resulting microstructure and determine the hardness.

There were five states in which the specimens were examined, including the initial as-built condition. Of the other four states, three were obtained by anneal cycles at increasing temperatures, 236 $^{O}$C, 406 $^{O}$C and 496 $^{O}$C (cf. the solidus and liquidus temperatures of ~ 542 $^{O}$C and ~ 580 $^{O}$C, respectively[42]). During these treatments the specimens were heated and cooled at rates of ± 100 $^{O}$C h$^{-1}$, and held at their annealing temperatures for ten hours. The final treatment comprised a two hour hold at 520 $^{O}$C and a water quench, followed by ageing for ten hours at 160 $^{O}$C and furnace cooling, again at -100 $^{O}$C h$^{-1}$. This is similar to the optimum precipitation hardening procedure determined for the closely related A356 alloy (6.5 - 7.5 wt.% Si) by Möller et al.[43]. The heat treatment conditions are provided in table 1.

**(Table 1)** {The sequence of heat treatments received by the SLM specimens.}

There has so far been little exploration of heat treatment procedures for Al-Si10-Mg produced by SLM. We chose to examine a range of anneal cycles as they are frequently used to relieve the residual stresses that arise from the SLM process and can cause part deformation. The final treatment was chosen to determine the effect of a conventional precipitation hardening procedure on SLM material which, as previously stated, possesses an inherently fine microstructure, providing hardness and strength that are in excess of conventionally manufactured material[19]. A range of heat treatments have been shown to provide increased ductility in the closely related alloy Al-Si12[27] and Ti-6Al-4V[18], both produced by SLM.

### 2.3 X-ray computed tomography - measurement

X-ray CT measurements were performed with an Xradia 500 Versa X-ray microscope (XRM). The source is an X-ray tube with a variable accelerating voltage from 30 to 160 kV; in this work an accelerating voltage of 60 kV was used. The X-rays pass through the sample and project a magnified image onto a scintillator screen. This produces visible wavelength photons which are focused onto a

2048 x 2048 element charge-coupled device (CCD). During imaging, the Al-Si10-Mg specimen was positioned at a distance of 12 mm from the X-ray source and 101 mm from the detector. A 4x objective lens was used to focus the radiographs onto the CCD. The images presented here were then reconstructed from the radiographs by filtered back-projection. The pixel size was 3.58 µm, which, by comparison with the results of Tammas-Williams et al.[41] for EBM Ti-6Al-4V, offered sufficient precision to examine the expected pore size distribution. The theoretical maximum spatial resolution offered with this set-up was 1.8 µ m $px^{-1}$ but, as highlighted by Tammas-Williams et al.[41], and discussed elsewhere[44-46], this is difficult to define accurately and is affected by several factors, of which beam hardening, centre of rotation determination, and penumbral blurring (due to the finite X-ray source size) are examples. The specimen was rotated around its z-axis in 1600 steps, with each orientation being exposed for 6 s. The number of images and exposure time of each determines the signal-to-noise ratio, and thus the clarity, of the final reconstructed CT images. The parameters used here were found to provide a low level of noise after preliminary trials with shorter exposure times.

**(Figure2)** {Convergence of the total porosity with number of sampled CT slices.}

### 2.4 X-ray computed tomography – analysis

X-ray CT image processing was performed using the public domain software ImageJ[47]. Each CT measurement provided a stack of images, each representing a cross-section in the *xy* plane with a layer thickness of 3.58 µm. A sample of 100 images, equally spaced throughout the vertical direction of the specimen, was taken to expedite the analysis procedure. The results of a convergence test for specimen porosity as a function of sampled CT layers are presented in figure 2; they show that this sampling level is sufficient to describe the porosity, as the difference between subsequent values in the convergence test was reduced to ~ 3% at the level of 100 analysed CT slices.

Regarding the processing of the individual sampled images, if required, a rotation transformation was performed so that the Cartesian frame of the image corresponded to that of the specimen, compensating for any small misalignment of the specimen with respect to the X-ray detector. The images were then cropped so that only the specimen interior remained for analysis. Lastly, a colour threshold was applied which discriminated between solid material and pores. These three processes are illustrated in figure 3, where the solid material and pores are represented as white and black, respectively, in the thresholded images.

For the purposes of this work, the colour thresholding, or segmentation, process was identified as the most critical aspect of the CT image analysis, as it introduces uncertainties into the size and shape descriptors of the analysed pores. We implemented the maximum entropy thresholding of Kapur et al.[48]. In section 3.3 we discuss the effects of minor variations in this automatic threshold approach on the pertinent quantities resulting from our analysis.

**(Figure 3)** {The rotation, cropping and colour thresholding process used on each sampled CT layer allowing the porosity to be quantified.}

The relative density of each sampled CT layer was determined by pixel counting, that is, the number of black pixels, representing pores, divided by the total number of pixels in the image. A representative density for the volume of the specimen was obtained by summing all of the pores and dividing by the total examined cross-sectional area. This is an improvement on the way in which the relative density of SLM parts is traditionally obtained from a small number of optical micrographs, which can take a long time to prepare and are often unrepresentative of the whole specimen due to the small number of sampled pores. For example, optical microscopy of our cross-sectioned specimens provided porosity values in the range of 0.17% to 0.25%, while the values from CT, averaging over the whole specimen, were considerably smaller, at 0.06% to 0.07%. The CT porosity convergence test in figure 2 shows that these are robust values. The difference between these results can be

explained by the examination of layers with above average porosity for the optical microscopy method; as can be seen in figures 4(b) and (c), which show the porosity and average pore area of each layer in the build direction, this is not unlikely, as the presence of a small number of larger pores can significantly increase the apparent porosity of a randomly exposed layer, with the highest porosity for a single CT layer seen here to be 0.47%. Another factor contributing to the difference between the microscopy and CT porosity results is that the latter may be insensitive to the presence of smaller pores, below a manually defined size threshold (see section 3.1). This issue has been discussed by Spierings et al.[36], who concluded that, while this constituted a disadvantage for the CT method of porosity evaluation, its main advantage is the examination of the pores' spatial distribution in three dimensions.

Pore areas were also obtained with a pixel counting method, with each black pixel inside a pore contributing an area of 12.82 μm$^2$, i.e.(3.58 μm)$^2$. Each pore was characterised with two shape descriptors; the pore circularity and aspect ratio. The first, $f_{circ.}$, is defined as

$$fcirc. = \frac{4\pi A}{p^2} \qquad (1)$$

where $A$ and $P$ are the cross-sectional area and perimeter of the pore, respectively. Thus, $f_{circ}$ can take values $0 < f_{circ} \leq 1$, where 1 represents a perfect circular cross-section. The second descriptor is given by

$$faspect = \frac{d_{min}}{d_{max}} \qquad (2)$$

where $d_{min}$ and $d_{max}$ are the minimum and maximum orthogonal axis of the best fitting ellipse to the pore. Once again, $f_{aspect}$ can take values $0 < f_{aspect} \leq 1$.

This form of 2D pore analysis, repeated over a sufficient number of layers in the $z$ direction (determined by the convergence study presented above), is far less computationally demanding than a

3D approach where every layer is examined, and pore volumes, rather than cross-sectional areas, are determined. This is especially true of cases such as this investigation, in which the total sample volume (5 x 5 x 5 mm) is very much larger than the CT resolution, and the pores are relatively few and spatially well distributed. This was established in preliminary analyses which predicted a computational time of over 32 hours to determine the 3D pore characteristics in the whole volume of our sample, compared to the minute or so needed for the 2D analysis. Therefore, high resolution 3D pore analysis would be impractical even for small SLM components. This is important as, if this form of information-rich NDT is to be applied at an SLM component validation stage during the manufacturing process, it will have to operate on material volumes much larger than that used here. The data analysis should be as straightforward and time-efficient as possible in order to minimise material wastage through the scrapping of defect components. An additional benefit of the 2D slice approach is that it yields pore shape and size distributions which are directly comparable with those provided by conventional cross-sectioning and microscopy, therefore providing a clear means of validating the non-destructive CT method against a more well-established process. Finally, it is worth noting that, as yet, there exists no standardised method for the examination of metal porosity by CT measurements. 2D and 3D analysis approaches each have their merits when applied in different circumstances. The interested reader is directed to the works of Landron et al.[49-50], Gupta et al.[51], Weck et al.[52] and Toda et al.[53], which detail some applications of 3D metal porosity analysis.

### 2.5 Microstructure and hardness

At each stage of the heat treatment described above, a specimen was selected for cross-sectioning, optical microscopy, and hardness tests. The planes exposed by cross-sectioning were parallel to the build, i.e. *z*-, direction. The specimens were polished following the procedure proposed by Struers Ltd.[54], and etched with Keller's reagent (1% HF, 1.5% HCl, 2.5% HNO3, 95% H2O)[55] to reveal the grain boundaries. Hardness values were determined from an average of ten indentations per

sample, using a Vickers indenter with a load of 300 gf (2.94 N). Scanning electron microscopy (SEM) and energy-dispersive X-ray spectroscopy (EDX) were used to examine the distribution of Si particles in the SLM material in its final heat treated state.

## 3. Results and discussion

### 3.1 X-ray computed tomography

**(Figure 4)** {Numbers of pores (a), porosity (b), mean (c) and median (d) pore areas at increasing height in the SLM specimen in its as-built condition.}

Figure 4(a) shows the number of pores per sampled CT layer over the central 4 mm of height for the sample in the as-built condition. The mean is 9.2 pores per layer, or 42 pores per $cm^2$, and it can be seen that the distribution is not uniform; the number of pores per layer increases with specimen height. A first-order polynomial fit provided a gradient of $(1.1 \pm 0.4) \times 10^{-3}$ pores per layer per micrometre. Each CT layer contains, on average, approximately one additional pore than a layer sampled 1 mm below. There is, therefore, some evidence for an increasing rate of pore formation throughout the SLM process. However, as can be seen in figure 4(b), the level of porosity throughout the sample did not increase in the same way. The main features of note in figure 4(b) are the peaks in layer porosity. These correspond to sequences of sampled layers in which the same large pore or pores featured, i.e. resampling of the same pores, which is illustrated in figure 5. We see evidence for this in the mean pore areas in figure 4(c), which shows that pores with larger cross-sectional areas are responsible for the variations in porosity. Figure 4(c) shows that the *z*-axis separation between these large pores varies significantly, and can reach up to 400 μm. The median pore areas are presented in figure 4(d). Compared to the mean values these are less sensitive to the presence of very large pores, and so show smaller variation. Given the total distribution of pore areas in the specimen, which is discussed shortly, the median values provide a better representation of average pore size.

**(Figure 5)** {Resampling of larger, inter-layer, pores across multiple CT layers.}

These observations have implications for the future application of X-ray CT in SLM part validation and process monitoring; analysing porosity and pore size as a function of build height, which in SLM is associated with a specific time in the manufacturing process, provides a means to correlate observed defects with known processing issues. For example, an inspected region of high porosity might be seen to coincide with a recorded fluctuation in the laser power, and gradually increasing porosity could indicate a problem with drifting laser focus due to thermal effects in the focussing optics or contamination of the window to the SLM chamber through which the laser passes. As for the high porosity and large pore area features observed in figures 4(b) and (c), they are randomly distributed in the z direction, indicating that the generation of the large pores was also random over processing time.

**(Figure 6)** {All sampled pores in the SLM specimen projected onto a single *xy* plane. The relative point sizes are representative of each pore area, but they are not to scale. The data points are also coloured to indicate pore area. The *x* and *y* projected histograms represent pore numbers over the sampled volume.}

Figure 6 provides the positions of all the observed pores throughout the volume of the specimen, again in its as-built condition, projected onto a single *xy* plane. The largest pores were clustered generally within a ~ (3 x 3) mm region towards the centre of the specimen, with almost no large pores present outside that region. The distribution of smaller pores extends to the edges of the specimen, and there are two pockets of small pores observed in the $y \sim 0$ μm corners.

The region of reduced pore size may be associated with a decreased cooling rate of the melt pools at the outside edges of the part due to the proximity of the feedstock powder, which, with its interstitial air-filled voids and small contact areas between particles, is more insulating than the consolidated

material towards the center of the specimen[56,57]. This is the interpretation previously suggested by Spierings et al.[36] for a similar observation in SLM stainless steel 316L. Conversely, other work on Al-Mg-Si alloys by Kim et al.[58] and Al-Mg alloy by Fang et al.[59] has shown that larger pores result from lower cooling rates.

The generation of large pores may also be related to in-process surface defects, such as balling[23,60,61] and laser spatter[62], which are occur at the topmost surface, i.e. the layer currently being processed, throughout SLM part production. Surface roughness results in the non-uniform spreading of feedstock powder after each laser scan, and this affects the laser-surface interaction. Balling, in particular, which has been observed in the production of various SLM materials including Al-Si10-Mg[23,60,61], may play a crucial role in pore generation; it was previously observed that a pre-sinter scanning strategy, in which the feedstock powder was subject to two laser scans, the first with half the power of the second, resulted in layers with lower roughness, lower part porosity and far fewer large pores than was achieved otherwise[23].

**(Figure 7)** {Histograms representing the pore areas and (inset) diameters for the SLM specimen in the as-built condition. Also shown for the diameter distribution is the Weibull probability density function (PDF) fit.}

In figure 7 is a histogram representing the pore areas in the sampled volume of the specimen in its as-built condition, while an inset shows the diameters. An equivalent diameter based on circular cross-sections was used, though the pores actually deviate from ideal spheres, as will be discussed shortly. The distributions are continuously increasing toward small pore size. It is worth noting at this stage that during image analysis a minimum feature size threshold can be specified, below which the pores are not counted. The purpose of this is to exclude the effects of low level experimental noise, which is unavoidable regardless of X-ray image exposure time, on the final descriptive statistics. The smallest possible pore that could arise from noise would be one pixel, or 12.82 $\mu m^2$ given the resolution achieved here. To ensure that all such noise was excluded from the statistics, a size

threshold of 2 x 2 pixels, or 51.27 μm$^2$, was employed. Therefore, from the X-ray CT data alone, we cannot compare the low end pore size distributions with results from Pavanti et al.[38],and Chawla and Deng[40]. Those authors used optical microscopy to examine the pores in sintered iron and steel, and observed dips at the low end of the pore size distributions, below ~ 5μm in diameter and ~ 15μm$^2$ in area, respectively. These are characteristic of Weibull distributions of pore diameters. Shen et al.[39], and Williams and Garner[35], found similar features, albeit at larger pore diameters, in their analyses of titanium and ceramic foams. 95% of the pores observed here were below 100μm in diameter (see figure 8), a finding in good agreement with the results of Tammas-Williams et al.[41] for Ti-6Al-4V made by EBM.

**(Figure 8)** {Cumulative frequency (normalised to unity) of the pore diameters in the sample in its as-built condition.}

A Weibull probability density function (PDF) was used to describe the observed pore diameters. This was chosen as it was previously employed by Shen et al.[39] in their examination of pore diameters, and it is known to have a theoretical basis for the description of flaws in materials[63,64]. The form of the Weibull PDF is provided in table 2, where *N* is the normalised pore frequency and *d* is the pore diameter. Also provided in table 2 are the relevant parameters and goodness-of-fit indicators (reduced R-squared and root mean squared error (RMSE) values) resulting from the fit. Robust fitting was implemented, with bisquare error weightings.

**(Table 2)** {The form, parameters and goodness-of-fit indicators of the Weibull PDF used in the fitting of the pore diameter distribution (see figure 7) in the as-built condition. *N* is the normalised frequency of pores and *d* is the pore diameter.}

The shape parameter, *m*, determined from our Weibull fitting was close to 1, meaning that the Weibull fit behaved very much like a decaying exponential distribution, i.e. $N(d) \propto e^{(-d/c)}$. This is in contrast to the work of Shen et al.[39], where m were in the range 2.3 - 2.5. The difference in these quantities

is due to a difference in the size distributions of the pores, which is expected because Shen et al.'s[39] foamed titanium and the SLM aluminium here were manufactured by quite different processes, and therefore the pore formation mechanisms were not alike. There is the possibility that the SLM material's pore size distribution exhibits a characteristic Weibull dip at low values but, due to the lack of sensitivity to the smallest pores in the specimens, because of the resolution and thresholding issue discussed above, it is not evident. Without a dip to small numbers of small pores, the $(d/c)^m$ term in the Weibull model, which is a growth term for positive values of $m$, cannot be significant, and therefore $m$ must be close to 1.

Using the Weibull model it was found that the pore diameter distributions from the various heat treatment conditions were effectively described by the same PDF as the as-built condition, with some small variations in fit parameters. We can deduct from this that the heat treatments had little effect on the distribution of pore sizes, and this is confirmed by the evidence in figure 9. The box plots in figure 9(b), which represent the lower quartile ($A_{LQ}$), median ($\tilde{A}$) and upper quartile ($A_{UQ}$) values for the pore area distribution in each state, show no evolution in pore size. The $A_{LQ}$, $\tilde{A}$ and $A_{UQ}$ representation is more meaningful than a mean and associated standard error, because the pore size distributions, being so heavily skewed towards small values, are not Gaussian.

Over the same course of heat treatments the relative density of the part (figure 9(a)) was also uniform, with a mean value of (99.93 ± 0.01)%. This consistency was to be expected since, in the event of pore formation, agglomeration or morphology changes, the ratio of solid material to void would stay constant. Only a thermo-mechanical process such as hot isostatic pressing (HIP) is likely to affect the relative density, through plastic deformation and pore closure[65-67].

**(Figure 9)** {Pore properties for the SLM specimen obtained after subsequent heat treatments (which are denoted in sub-figure (a) and described in table 1. Mean CT densities are provided in (a). Median, upper

quartile and lower quartile values for pore areas, circularities and aspect ratios are shown in (b), (c) and (d), respectively.}

Figures 9(c) and (d) show the pore circularities and aspect ratios over the range of heat treatments. As for the pore areas discussed above, the $f_{circ.}$ and $f_{aspect}$ distributions (see figure 10) are not well described by a single mean with a standard error. For this reason, their distributions are best represented as $f_{LQ.}$, $\tilde{f}$ and $f_{UQ}$ values also, from which we can see there is little pore shape variation and no trend over the full range of heat treatments.

**(Figure 10)** {Histograms and cumulative frequencies of circularity (a) and aspect ratio (b) of the pores in the as-built SLM specimen. These shape descriptors were defined in equations 1 and 2, respectively.}

In figure 10 we provide the distributions of the pore shape descriptors the $f_{circ.}$ and $f_{aspect.}$ Again, these come from the pores observed in the specimen in the as-built condition. The histograms show a broad range of both aspect ratio and circularity, but the latter, which is an indicator of the smoothness of the perimeter of each pore, has a skewed distribution tending toward higher values with a peak at ~ 0.85. The $f_{circ.}$ and $f_{aspect}$ distributions are similar to those obtained by Pavanti et al.[38] in sintered iron using optical microscopy. Note that the histograms in figure 10 provide shape information which is insensitive to the size of the pores; other informative plots, in which pore sizes are considered also, are provided in section 3.2.

**(Figure 11)** {Selected regions from a single CT slice of the SLM specimen in the as-built (a) and (c), and precipitation hardened (b) and (d), conditions. The pairs of sub-figures show the same pores, which contains some unmelted and unconsolidated powder (including one powder particle with an interior void).}

Lastly, figure 11 provides fairly clear evidence that the examined pores have been unaffected by the range of heat treatments applied here. In figures 11(a) and (c) are CT cross-sections of large, irregular

pores. The pores enclose several particles of feedstock powder (one of which can be seen to include an interior void), which are thought to be partially sintered to the pore interior surfaces. Figures 11(b) and (d) show the same pores as (a) and (c) after the full range of heat treatments including 2 hours at 520 $^{O}$C; the powder particles remain and are found in the same locations. The small differences in pore geometry between 11(a) and (b), and (c) and (d), are believed to be due to the unavoidable small misalignment of the sample in the X-ray microscope in each condition, therefore causing the pores to be observed from fractionally different angles in each case, rather than morphological changes. This error is estimated to be of the order ± 3$^{O}$ in the inclination of the specimen with respect to the source and detector.

### 3.2 Pore anisotropy

**(Figure 12)** {Pores (dark regions) in the SLM specimen, observed along the three principal axis and in 3D projection.}

The statistics above were obtained from analysis of the CT image stack which, as previously mentioned, comprises a series of images in the *xy* plane. There may therefore be some sampling bias in the shape and size descriptors if the pores possess large anisotropy. This was examined by reconstructing a full three-dimensional representation of the specimen pores from the CT data. The result is shown in figure 12, where three orthogonal views of the pores in the as-built condition are provided. Visual inspection is sufficient to deduce that there is, indeed, significant anisotropy in the shapes of the pores; the larger pores are relatively flat or disc-like in the *xy* plane, providing long, thin profiles when viewed in the *yz* and *zx* planes. There is more quantitative evidence for this in figure 13, where the aspect ratio of the pores is expressed as a function of the pore size for the *xy* and *zx*

planes. In the *xy* plane we see a large number of large pores with a range of aspect ratios extending to quite high values, i.e. more circular. In contrast, the same pores viewed in the *zx* plane have much lower size, not exceeding ~ 2 x $10^4$ μm$^2$, and have aspect ratios tending toward low values, i.e. more eccentric ellipses. The strong anisotropy of the largest pores is believed to be related to the layerwise manufacturing process of SLM, and we speculate that the roughness of each melted layer, and the even distribution of feedstock powder before melting, are critical if these undesirable pores are to be reduced, or indeed eliminated, from SLM parts.

**(Figure 13)** {Pore aspect ratios as a function of pore area for pores viewed in the *xy* plane (left) and *zx* plane (right).}

### 3.3 CT image thresholding

As mentioned previously, each of the pore size and shape descriptors resulting from the statistical analyses presented here are influenced by the choice of colour thresholding method for the CT images. For each image, the greyscale threshold was determined by the maximum entropy method of Kapur et al.[48]. We explored the effect of manually adjusting the upper limit of the automatic threshold value by ± 5% to determine which parameters were most affected. We found that the resulting uncertainty in the median shape descriptors $\tilde{f}_{circ.}$ and $\tilde{f}_{aspect}$ was approximately equal to the size of the thresholding change, around ± 5%. More affected was the mean value of porosity for the full image stack, which was altered by ± 10% from the value it had when the automatic thresholding level was used. Finally, the median pore area, $\tilde{A}$, was altered by $\frac{-24}{+14}$ % for the same ± 5% change in threshold value. These significant and unequal variations are due principally to the inclusion and exclusion into the descriptive statistics of large numbers of relatively small pores when the threshold level is increased and decreased, respectively. This issue is highlighted as an area for future investigation in the concluding section of this work.

### 3.4 Microstructure and hardness

**(Figure 14)** {Optical micrographs of polished and etched SLM specimens following subsequent heat treatments. Sub-figures (a) through (e) relate to the heat treatments described in table 1. Regions of lighter and darker contrast are α-phase Al and silicon particles, respectively.}

The microstructural evolution of the specimens is shown in figure 14, where the characteristic SLM melt pools in the as-built condition, which are delineated by the transition from a fine to coarse cellular-dendritic structure[19,20], give rise to a coarse structure of agglomerated Si particles after heat treatment. The mechanism behind this transformation has been described by Prashanth et al.[27] for Al-Si12 produced by SLM. At low annealing temperatures the Si diffuses out of the Al-Si matrix to form small particles. With increasing temperature these agglomerate, forming exponentially larger particles and eliminating the melt pool boundaries. Figure 15 shows that the dark flakes observed with optical microscopy correspond to Si concentrations determined by energy-dispersive X-ray spectroscopy (EDX) mapping at the Si $K\alpha_1$ X-ray emission energy.

**(Figure 15)** {SEM (a) and EDX (b) imaging of the SLM specimen in its final, precipitation hardened, state. The image presented in (b) shows EDX mapping in the same region as (a), obtained at the Si $K\alpha_1$ X-ray emission energy - the dark features are Si particles.}

In the final state, following the 520 $^{O}$C solution heat treatment and artificial ageing at 160 $^{O}$C, the mean diameter of the Si particles was (1.61 ± 0.01) μm and their spatial density was (87.0 ± 0.1) x $10^{-3}$ Si particles per $\mu m^2$. These values conform well to those ultimately obtained for SLM Al-Si12 by Prashanth et al.[27].

**(Figure 16)** {Vickers hardness (HV) values obtained from multiple measurements of the SLM specimens under 300 gf (2.94 N) after subsequent heat treatments. The error bars of the last three data points are smaller than the symbols.}

The corresponding Vickers hardness for each of the heat treatment conditions are provided in figure 16. Annealing cycles at increasing temperatures reduced the initial as-built hardness from (114 ± 3) HV, which is in reasonable agreement with previous results[19], to a value of (45.2 ± 0 .7) HV. This increased to (59 ± 1) HV after the precipitation hardening process. These observations are consistent with the microstructure coarsening effect of the annealing cycles, which allows easier dislocation motion, and the subsequent growth of hardening β(Mg2Si) precipitates[43,68].

## Conclusions

X-ray computed tomography was used to investigate the interior pores of the alloy Al-Si10-Mg produced by SLM. A range of post-manufacture heat treatments, which we have shown to significantly alter the microstructure and hardness of the SLM material, have no measurable effect on the porosity; the quantity of pores, and their shapes, sizes and positions were unaffected. Therefore, since the performance and failure mechanisms of parts depend upon both the microstructure and porosity, efforts should be undertaken to robustly determine the pore formation mechanisms in SLM, so that their presence can be minimised in future parts. For this objective, the finding that the largest pores in the SLM material are strongly anisotropic, being flat and disc-like in the *xy* plane, is important, because the planes of these pores correspond to the planes of the layerwise manufacturing process.

The data made available by the CT method has been demonstrated in the quantitative analyses of the spatial, size and shape distributions of the pores. Distributions of this statistical quality cannot be obtained by conventional cross-sectioning and microscopy because the required number of micrographs would be prohibitively large. The methodology and findings have implications for; (i) SLM part validation - checking that pores are well distributed, so as to retard crack initiation and

growth, or checking that pores are limited to non-critical regions of parts, (ii) process development - the refinement of scanning strategies to avoid the generation of large, irregular, pores, (iii) failure probability analysis - through comparison with the Weibull distribution of pore diameters, and (iv) lifecycle modelling - through the determination of crack growth rates for specified applications based on accurate pore populations.

On the basis of the results presented here, there are three main areas in which further work may yield improvements to the understanding, and the implementation, of SLM part production. First, the relationship between the rate of pore formation and the thermal properties of the melt pool environment is of some importance, as it has implications for optimum part design and process control. Second, the inhomogeneous distribution of pores seen here could be used to inform novel processing approaches that minimise the generation of large pores; these could take the form of geometry-dependent scanning strategies, or laser pulse modulation, as suggested by Zhou and Tsai[69] for the prevention of porosity in laser welding. Lastly, for pore morphologies in SLM parts to be determined reliably, and in such a way as to be comparable with the work of other researchers or across industrial sectors, robust image analysis procedures which consider the effects of colour thresholding should be developed and adopted. Efforts in this regard are underway in our own group. Future investigations will examine the tensile and compressive behaviour of the as-built and heat treated SLM material to determine the effect of the altered microstructure on the macroscopic mechanical properties.

## Acknowledgments

Funding was provided by Innovate UK, formerly the UK Technology Strategy Board (TSB). Thanks to Mark East, Mark Hardy and Joe White, technicians of the Additive Manufacture and 3D Printing Research Group, and also to Tom Buss, who assisted with sample annealing.

## References

1. I. Gibson, D. W. Rosen, B. Stucker, *Additive Manufacturing Technologies: Rapid Prototyping to Direct Digital Manufacturing*, Springer, 2010.

2. N. Hopkinson, R. Hague, P. Dickens (Eds.), *Rapid Manufacturing: An Industrial Revolution for the Digital Age*, Wiley, 2005.

3. A. Aremu, I. Ashcroft, R. Wildman, R. Hague, C. Tuck, D. Brackett, *The effects of bidirectional evolutionary structural optimization parameters on an industrial designed component for additive manufacture*, P. I. Mech. Eng. B- J. Eng. 227 (2013) pp. 794-807.

4. G. Chahine, P. Smith, R. Kovacevic, *Application of Topology Optimization in Modern Additive Manufacturing*, in: Solid Freeform Fabrication Symposium (2010) pp. 606-618.

5. D. Brackett, I. Ashcroft, R. Hague, *Topology Optimization for Additive Manufacturing*, in: Solid Freeform Fabrication Symposium (2011) pp. 348-362.

6. N. Gardan, *Knowledge Management for Topological Optimization Integration in Additive manufacturing*, Int. J. Manuf. Eng. (2014).

7. J. Brennan-Craddock, D. Brackett, R. Wildman, R. Hague, *The design of impact absorbing structures for additive manufacture*, J. Phys.: Conference Series 382 (2012) pp. 12042-12049.

8. D. Brackett, I. Ashcroft, R. Wildman, R. Hague, *An error diffusion based method to generate functionally graded cellular structures*, Comput. Struct. 138 (2014) 102-111.

9. C. Yan, L. Hao, A. Hussein, D. Raymont, *Evaluations of cellular lattice structures manufactured using selective laser melting*, Int. J. Mach. Tool Manu. 62 (2012) pp. 32-38.

10. C. Yan, L. Hao, A. Hussein, P. Young, D. Raymont, *Advanced lightweight 316L stainless steel cellular lattice structures fabricated via selective laser melting*, Mater. Design 55 (2014) pp. 533-541.

11. C. Yan, L. Hao, A. Hussein, S. L. Bubb, P. Young, D. Raymont, *Evaluation of light-weight AlSi10Mg periodic cellular lattice structures fabricated via direct metal laser sintering*, J. Mater. Process Tech. 214 (2014) pp. 856-864.

12. N. A. Fleck, V. S. Deshpande, M. F. Ashby, *Micro-architectured materials: past, present and future*, Proc. R. Soc. A 466 (2010) pp. 2495-2516.

13. M. Smith, Z. Guan, W. Cantwell, *Finite element modelling of the compressive response of lattice structures manufactured using the selective laser melting technique*, Int. J. Mech. Sci. 67 (2013) pp. 28-41.

14. C. Yan, L. Hao, A. Hussein, P. Young, J. Huang, W. Zhu, *Microstructure and mechanical properties of aluminium alloy cellular lattice structures manufactured by direct metal laser sintering*, Mat. Sci. Eng. A-Struct. 628 (2015) pp. 238-246.

15. K. Ushijima, W. J. Cantrell, R. A. W. Mines, S. Tsopanos, M. Smith, *An investigation into the compressive properties of stainless steel micro-lattice structures*, J. Sandw. Struct. Mat. 13 (2011) pp. 303-329.

16. I. Maskery, A. Aremu, M. Simonelli, C. Tuck, R. Wildman, I. Ashcroft, R. Hague, *Mechanical Properties of Ti-6Al-4V Selectively Laser Melted Parts with Body-Centred-Cubic Lattices of Varying cell size*, Exp. Mech. 55 (2015) pp.1261-1272.

17. K. Wong, A. Hernandez, *A Review of Additive Manufacturing*, ISRN Mech. Eng. 2012.

18. B. Vrancken, L. Thijs, J.-P. Kruth, J. V. Humbeeck, *Heat treatment of Ti6Al4V produced by Selective Laser Melting: Microstructure and mechanical properties*, J. Alloy. Compd. 541 (2012) pp. 177-185.

19. K. Kempen, L. Thijs, J. Van Humbeeck, J.-P. Kruth, *Mechanical properties of AlSi10Mg produced by Selective Laser Melting*, Phys. Procedia 2009 (2012) pp. 439-446.

20. L. Thijs, K. Kempen, J.-P. Kruth, J. Van Humbeeck, *Fine-structured aluminium products with controllable texture by selective laser melting of pre-alloyed AlSi10Mg powder*, Acta Mater. 61 (2013) pp. 1809-1819.

21. M. Simonelli, Y. Y. Tse, C. Tuck, *Microstructure of Ti-6Al-4V produced by selective laser melting*, J. Phys.: Conference Series 371 (2012) pp. 12084-12088.

22. M. Simonelli, Y. Tse, C. Tuck, *Effect of the build orientation on the mechanical properties and fracture modes of SLM Ti6Al4V*, Mat. Sci. Eng. A-Struct. 616 (2014) pp. 1-11.

23. N. T. Aboulkhair, N. M. Everitt, I. Ashcroft, C. Tuck, *Reducing porosity in AlSi10Mg parts processed by selective laser melting*, Additive Manufacturing 1–4 (2014) pp. 77-86.

24. P. Mercelis, J.-P. Kruth, *Residual stresses in selective laser sintering and selective laser melting*, Rapid Prototyping J. 12 (2006) pp. 254-265.

25. N. Read, W. Wang, K. Essa, M. Attallah, *Selective laser melting of AlSi10Mg alloy: Process optimisation and mechanical properties development*, Mater. Design 65 (2015) pp. 417-424.

26. P. Ma, K. Prashanth, S. Scudino, Y. Jia, H. Wang, C. Zou, Z. Wei, J. Eckert, *Influence of Annealing on Mechanical Properties of Al-20Si Processed by Selective Laser Melting*, Metals 4 (2014) pp. 28-36.

27. K. Prashanth, S. Scudino, H. Klauss, K. Surreddi, L. Löber, Z. Wang, A. Chaubey, U. Kühn, J. Eckert, *Microstructure and mechanical properties of Al–12Si produced by selective laser melting: Effect of heat treatment*, Mat. Sci. Eng. A-Struct. 590 (2014) pp. 153-160.

28. M. Shiomi, K. Osakada, K. Nakamura, T. Yamashita, F. Abe, *Residual Stress within Metallic Model Made by Selective Laser Melting Process*, CIRP Annals - Manufacturing Technology 53 (2004) pp. 195-198.

29. M. Zaeh, G. Branner, *Investigations on residual stresses and deformations in selective laser melting*, Prod. Engineer. 4 (2010) pp. 35-45.

30. J. W. McPherson, C. F. Dunn, *A model for stress-induced metal notching and voiding in very large-scale-integrated Al–Si (1%) metallization*, J. Vac. Sci. Technol.: B 5 (1987) pp. 1321-1325.

31. X. L. Izcara, A. G. Blank, F. Pyczak, P. Staron, S. Schumann, N. Huber, *Characterization and modelling of the influence of artificial aging on the microstructural evolution of age-hardenable AlSi10Mg(Cu) aluminium alloys*, Mat. Sci. Eng. A-Struct. 610 (2014) pp. 46-53.

32. G. Edwards, K. Stiller, G. Dunlop, M. Couper, *The precipitation sequence in Al–Mg–Si alloys*, Acta Mater. 46 (1998) pp. 3893-3904.

33. Y. Hangai, O. Kuwazuru, T. Yano, T. Utsunomiya, Y. Murata, S. Kitahara, S. Bidhar, N. Yoshikawa, *Clustered Shrinkage Pores in Ill-Conditioned Aluminum Alloy Die Castings*, Mater. T. JIM 51 (2010) pp. 1574-1580.

34. E. Solórzano, M. Rodríguez-Pérez, J. Reglero, J. de Saja, *Density gradients in aluminium foams: characterisation by computed tomography and measurements of the effective thermal conductivity*, J. Mater. Sci. 22 (2007) pp. 2557-2564.

35. A. M. Williams, C. P. Garner, *Measuring Pore Diameter Distribution of Gelcast Ceramic Foams from Two-Dimensional Cross Sections*, J. Am. Ceram. Soc. 91 (2008) pp. 3113-3116.

36. A. Spierings, M. Schneider, R. Eggenberger, *Comparison of density measurement techniques for additive manufactured metallic parts*, Rapid Prototyping J. 17 (2011) pp. 380-386.

37. T. Marcu Puscas, M. Signorini, A. Molinari, G. Straffelini, *Image analysis investigation of the effect of the process variables on the porosity of sintered chromium steels*, Mater. Charact. 50 (2003) pp. 1-10.

38. H. Pavanati, A. M. Maliska, A. Klein, J. Muzart, *Comparative study of porosity and pores morphology of unalloyed iron sintered in furnace and plasma reactor*, Mat. Res. 10 (2007) pp. 87- 93.

39. H. Shen, S. Oppenheimer, D. Dunand, L. Brinson, *Numerical modelling of pore size and distribution in foamed titanium*, Mech. Mater. 38 (2006) pp. 933-944.

40. N. Chawla, X. Deng, *Microstructure and mechanical behaviour of porous sintered steels*, Mat. Sci. Eng. A-Struct. 390 (2005) pp. 98-112.

41. S. Tammas-Williams, H. Zhao, F. Léonard, F. Derguti, I. Todd, P. Prangnell, *XCT analysis of the influence of melt strategies on defect population in Ti-6Al-4V components manufactured by Selective Electron Beam Melting*, Mater. Charact. 102 (2015) pp. 47-61.

42. M. Vončina, P. Mrvar, J. Medved, *Thermodynamic analysis of AlSi10Mg alloy*, RMZ - Materials and Geoenvironment 52 (2006) pp. 621-633.

43. H. Möller, G. Govender, W. E. Stumpf, *The T6 Heat Treatment of Semi-Solid Metal Processed Alloy A356*, Open Mater. Sci. J. 2 (2008) pp. 6-10.

44. S. Stock, *Recent advances in X-ray microtomography applied to materials*, Int. Mater. Rev. 53 (2008) pp 129-181.

45. E. Maire, P. J. Withers, *Quantitative X-ray tomography*, Int. Mater. Rev. 59 (2014) pp. 1-43.

46. J. Kruth, M. Bartscher, S. Carmignato, R. Schmitt, L. D. Chiffre, A. Weckenmann, *Computed tomography for dimensional metrology*, CIRP Annals - Manufacturing Technology 60 (2011) pp. 821-842.

47. C. A. Schneider, W. S. Rasband, K. W. Eliceiri, *NIH Image to ImageJ: 25 years of image analysis*, Nat. Methods 9 (2012) pp. 671-675.

48. J. Kapur, P. Sahoo, A. Wong, *A new method for gray-level picture thresholding using the entropy of the histogram*, Comput. Vision Graph. 29 (1985) pp. 273--285.

49. C. Landron, O. Bouaziz, E. Maire, J. Adrien, *Experimental investigation of void coalescence in dual phase steel using X-ray tomography*, Acta Mater. 61 (2013) pp. 6821-6829.

50. C. Landron, O. Bouaziz, E. Maire, J. Adrien, L. Lecarme, A. Bareggi, *Validation of void growth models using X-ray microtomography characterization of damage in dual phase steels,* Acta Mater. 59 (2011) pp. 7564-7573.

51. C. Gupta, H. Toda, T. Fujioka, M. Kobayashi, K. Uesugi, A. Takeuchi, Y. Suzuki, *Micro-pore development phenomenon in hydrogen pre-charged aluminium alloy studied using synchrotron X-ray micro-tomography,* Appl. Phys. Lett. 103 (2013) pp. 171902-171904.

52. A. Weck, D.S. Wilkinson, E. Maire and H. Toda, *Visualisation by X-ray tomography of void growth and coalescence leading to fracture in model materials,* Acta Mater. 56 (2008) pp. 2919-2928.

53. H. Toda, E. Maire, S. Yamauchi, H. Tsuruta, T. Hiramatsu, M. Kobayashi, *In situ observation of ductile fracture using X-ray tomography technique,* Acta Mater. 59 (2011) pp. 1995-2008.

54. http://www.struers.co.uk/resources/elements/12/104900/Application\%20Notes\\\%20Aluminium\%20English.pdf.

55. G. Vander Voort, *Metallography: Principles and Practice,* ASM International, 1999.

56. M. Alkahari, T. Furumoto, T. Ueda, A. Hosokawa, R. Tanaka, M. Abdul Aziz, *Thermal Conductivity of Metal Powder and Consolidated Material Fabricated via Selective Laser Melting*, Key Eng. Mat. 523-524 (2012) pp. 244-249.

57. L. Kowalski, J. Duszczyk, L. Katgerman, *Thermal conductivity of metal powder-polymer feedstock for powder injection moulding*, J. Mater. Sci. 34 (1999) pp. 1-5.

58. T. B. Kim, S. Suzuki, H. Nakajima, *Effect of Conditions of Unidirectional Solidification on Microstructure and Pore Morphology of Al-Mg-Si Alloys*, Mater. T. JIM 51 (2010) pp. 496-502.

59. Q. T. Fang, P. N. Anyalebechi, D. A. Granger, *Measurement of Hydrogen Porosity in Unidirectionally Solidified Aluminum Alloys, in: Light Metals,* The Minerals, Metals and Materials Society, 1988.

60. I. Yadroitsev, A. Gusarov, I. Yadroitsava, I. Smurov, *Single track formation in selective laser melting of metal powders*, J. Mater. Process Tech. 210 (2010) pp. 1624-1631.

61. K. Osakada, M. Shiomi, *Flexible manufacturing of metallic products by selective laser melting of powder*, Int. J. Mach. Tool Manu. 46 (2006) pp. 1188-1193.

62. M. Simonelli, C. Tuck, N. T. Aboulkhair, I. Maskery, I. Ashcroft, R. D. Wildman, R. Hague, *A Study on the Laser Spatter and the Oxidation Reactions During Selective Laser Melting of 316L Stainless Steel, Al-Si10-Mg, and Ti-6Al-4V*, Metall. Mater. Trans. A (2015) pp. 1-10.

63. J. B. Quinn, G. D. Quinn, *A practical and systematic review of Weibull statistics for reporting strengths of dental materials*, Dent. Mater. 26 (2010) pp. 135-147.

64. R. German, *Sintering: From Empirical Observations to Scientific Principles*, Butterworth-Heinemann, 2014.

65. B. Kellett, F. Lange, *Experiments on Pore Closure During Hot Isostatic Pressing and Forging*, J. Am. Ceram. Soc. 71 (1988) pp. 7-12.

66. M. Ohring, *Engineering Materials Science*, Academic Press, 1995.

67. M. Agarwala, D. Bourell, J. Beaman, H. Marcus, J. Barlow, *Post-processing of selective laser sintered metal parts*, Rapid Prototyping J. 1 (1995) pp. 36-44.

68. A. Gupta, D. Lloyd, S. Court, *Precipitation hardening processes in an Al-0.4%Mg-1.3%Si-0.25%Fe aluminium alloy*, Mat. Sci. Eng. A-Struct. 301 (2001) pp. 140-146.

69. J. Zhou, H.-L. Tsai, *Porosity Formation and Prevention in Pulsed Laser Welding*, J. Heat Transfer 129 (2006) pp. 1014-1024.

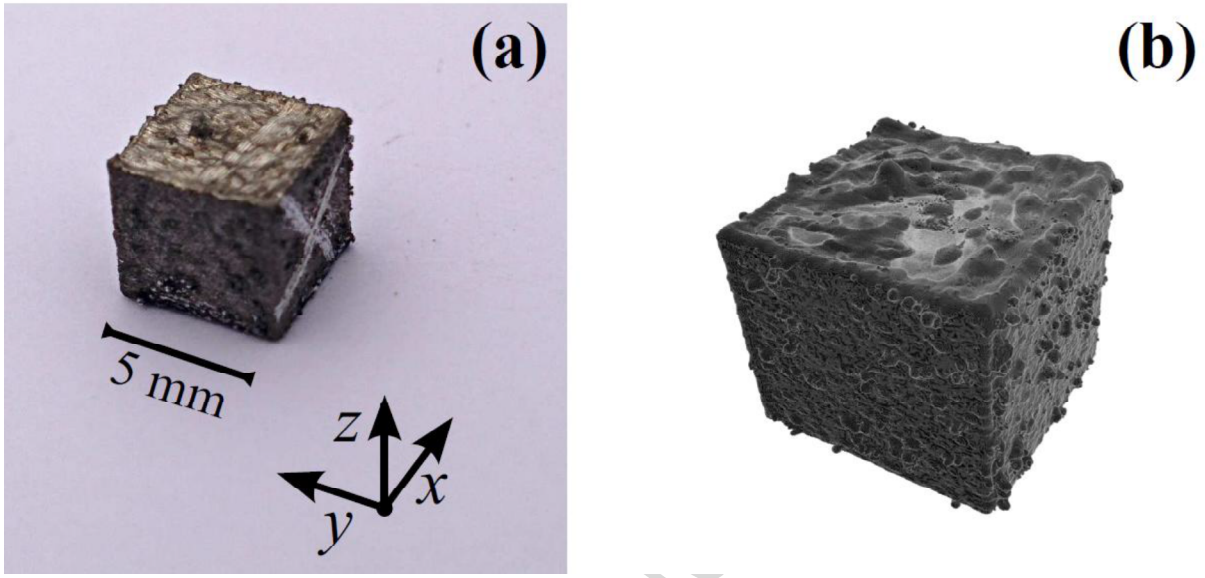


Fig. 1

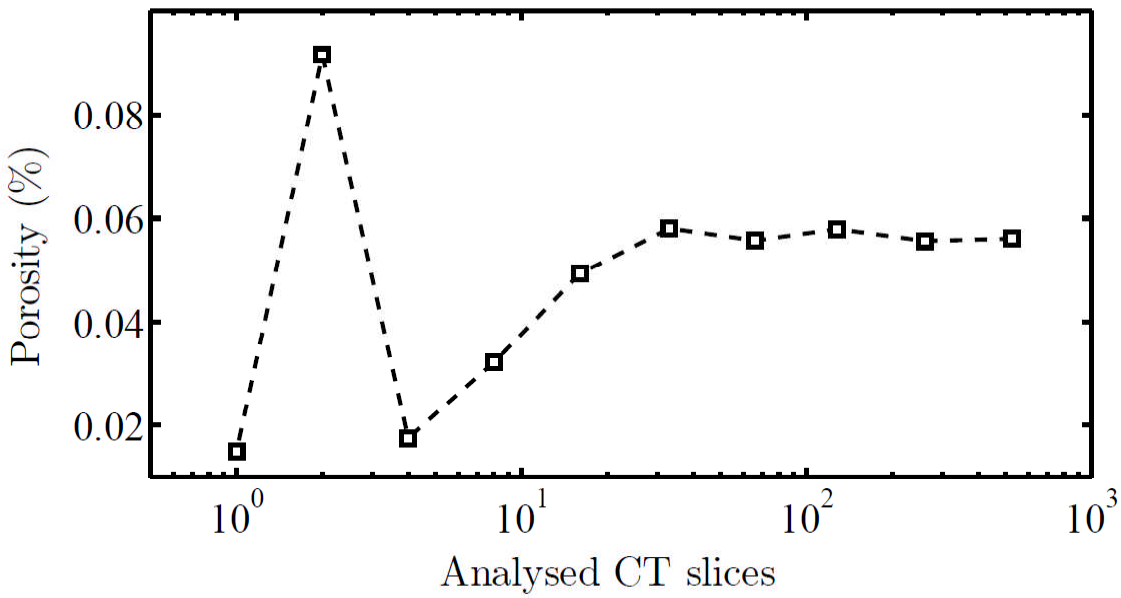


Fig. 2

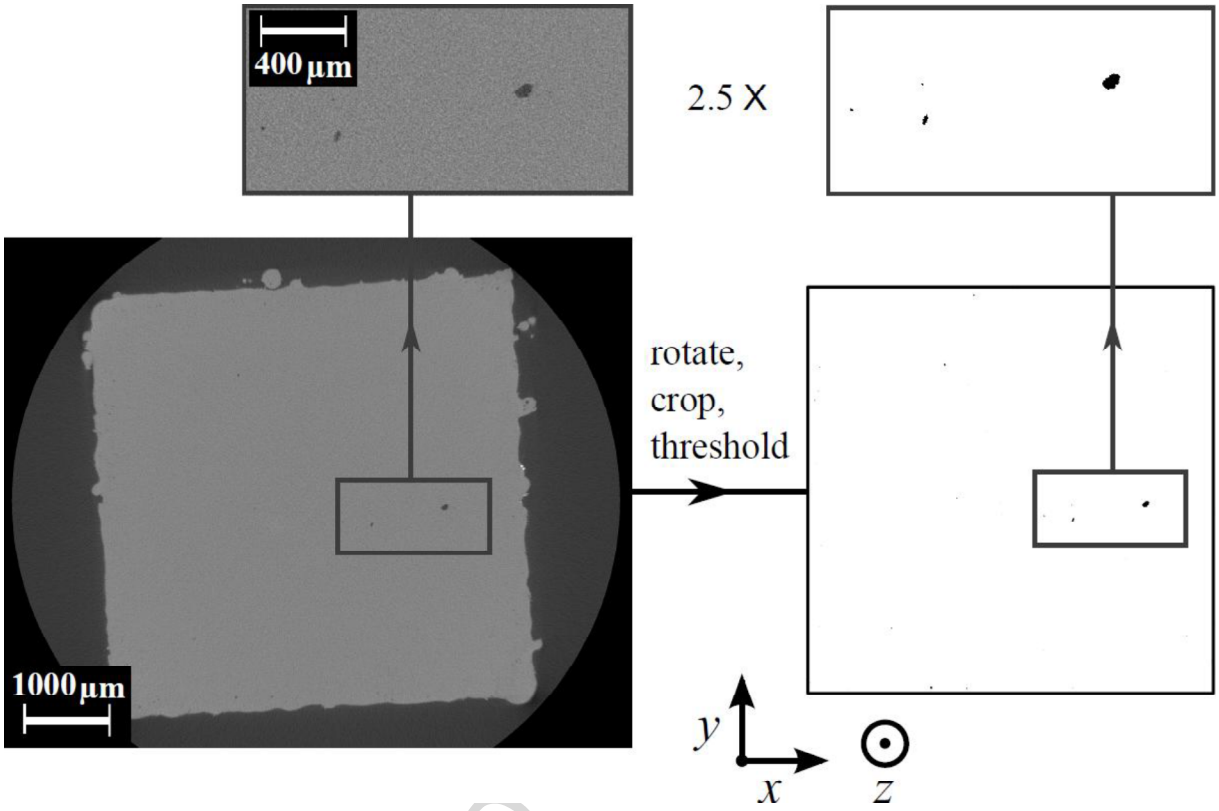


Fig. 3

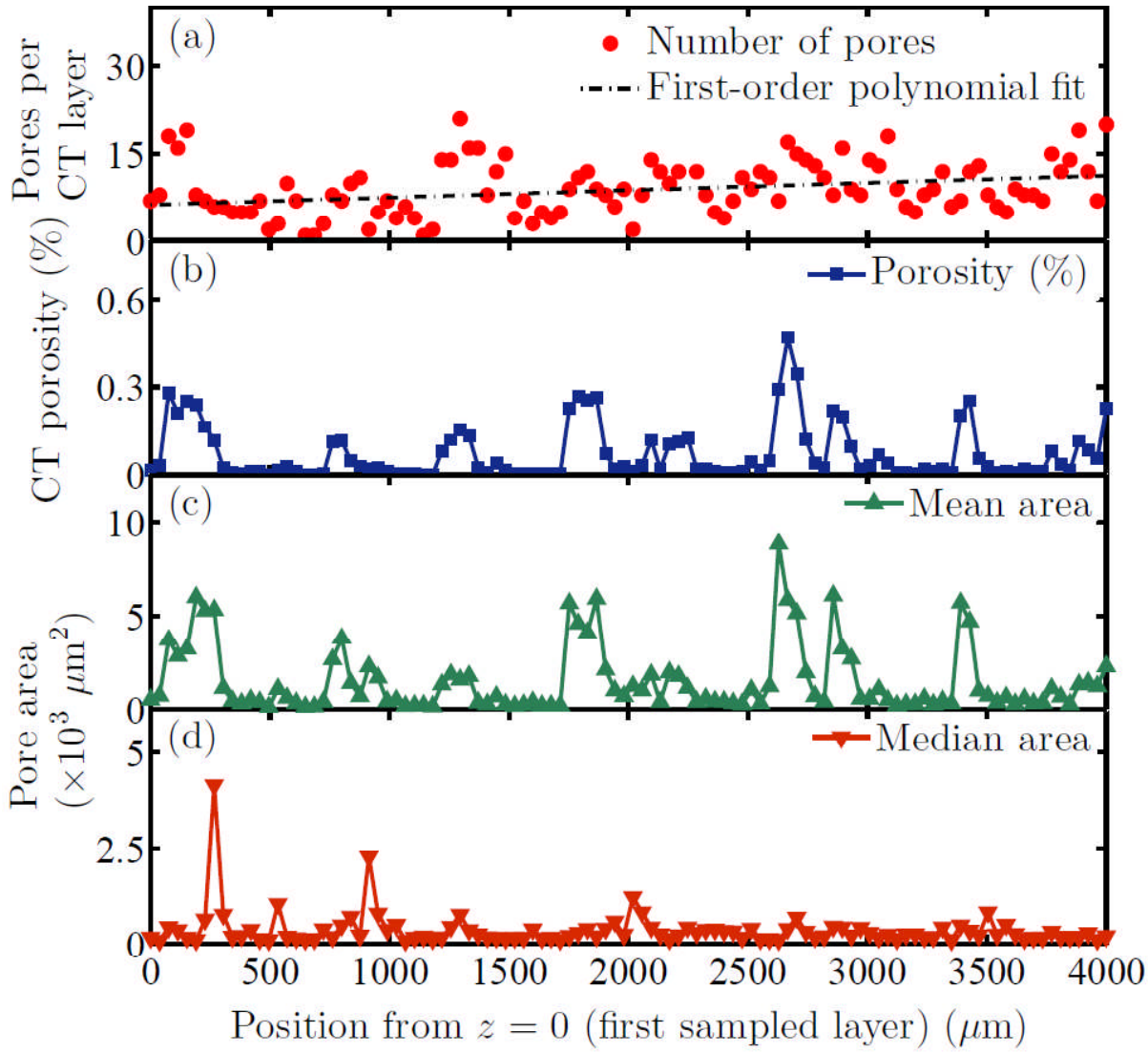


Fig. 4

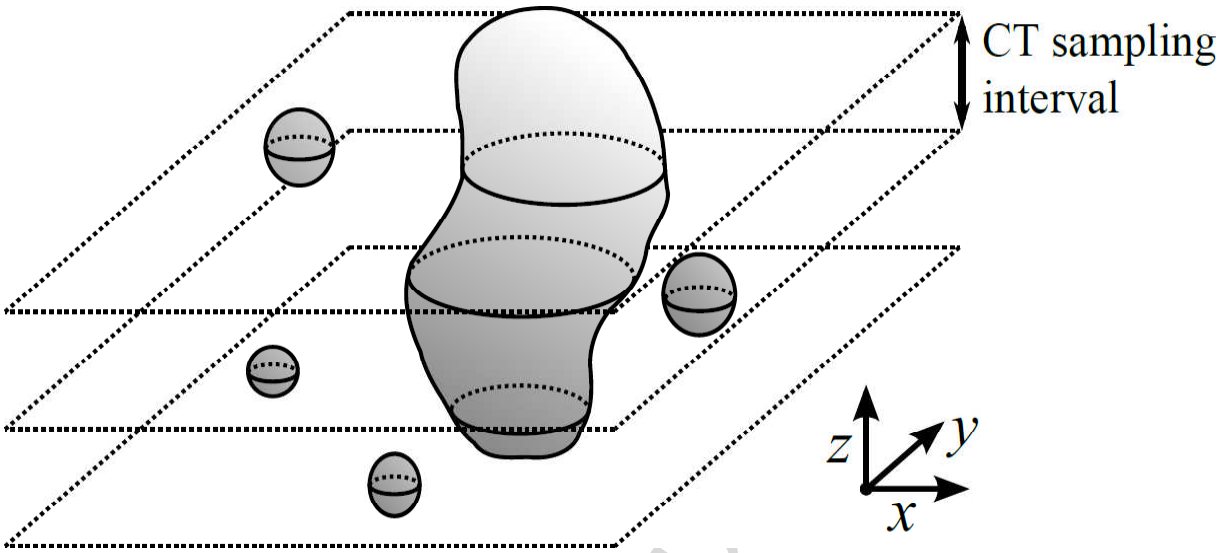


Fig. 5

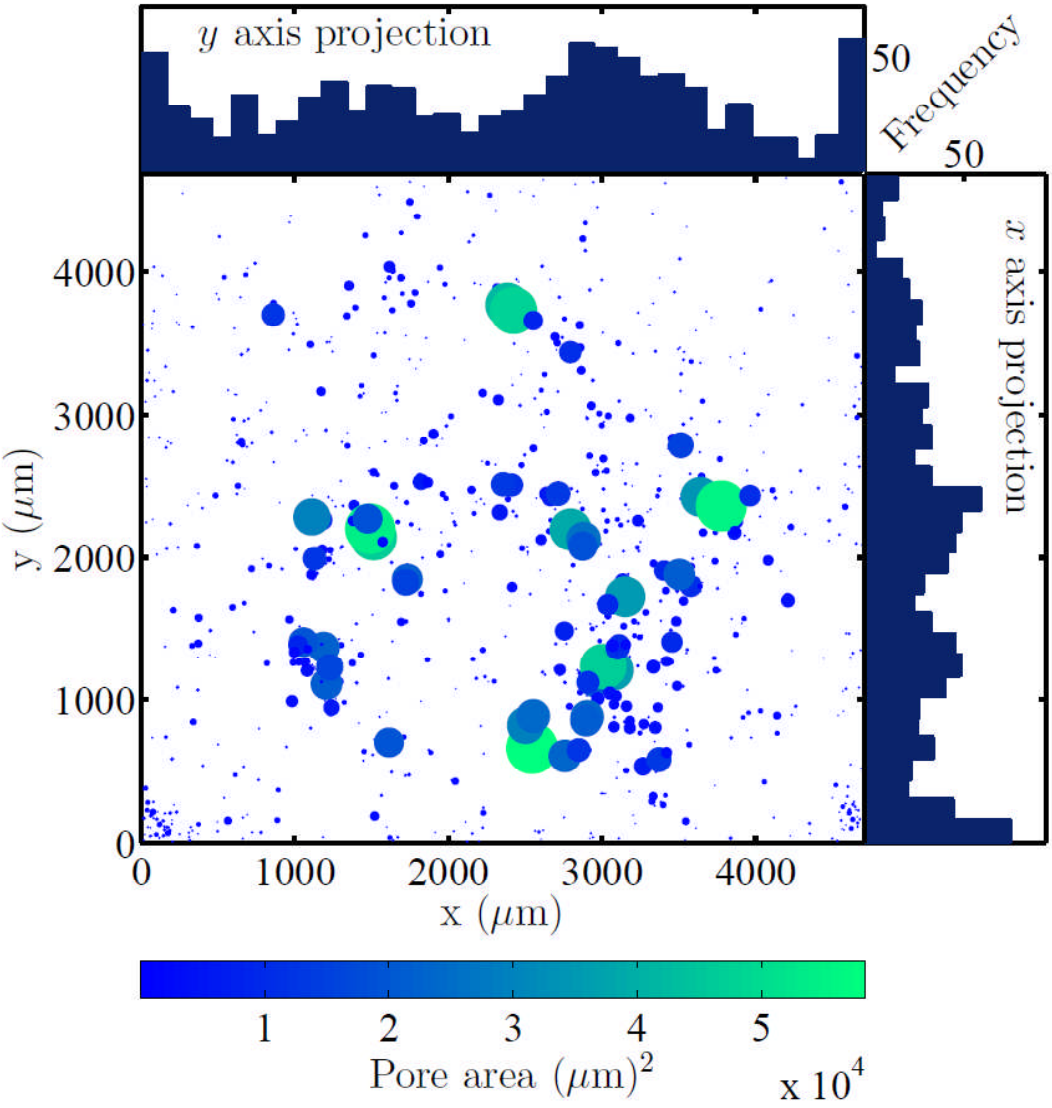


Fig. 6

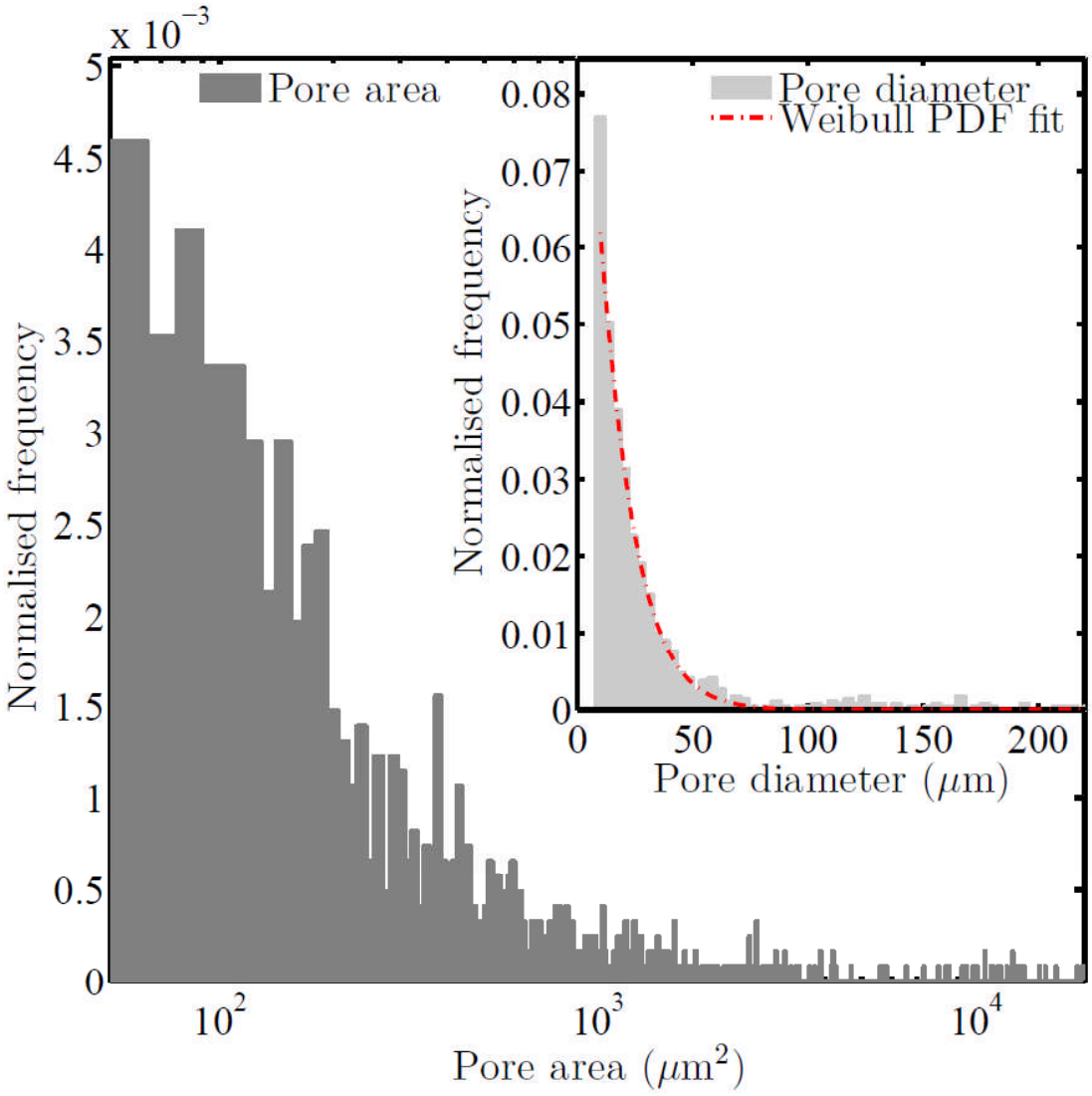


Fig. 7

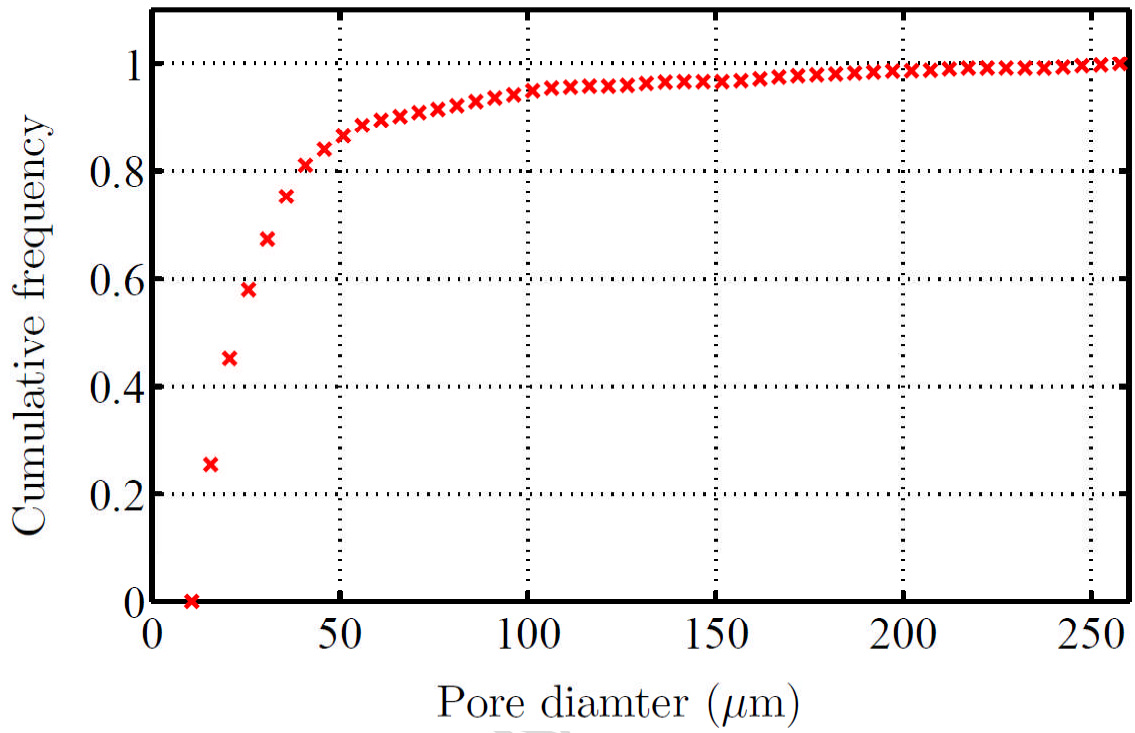

Fig.

8

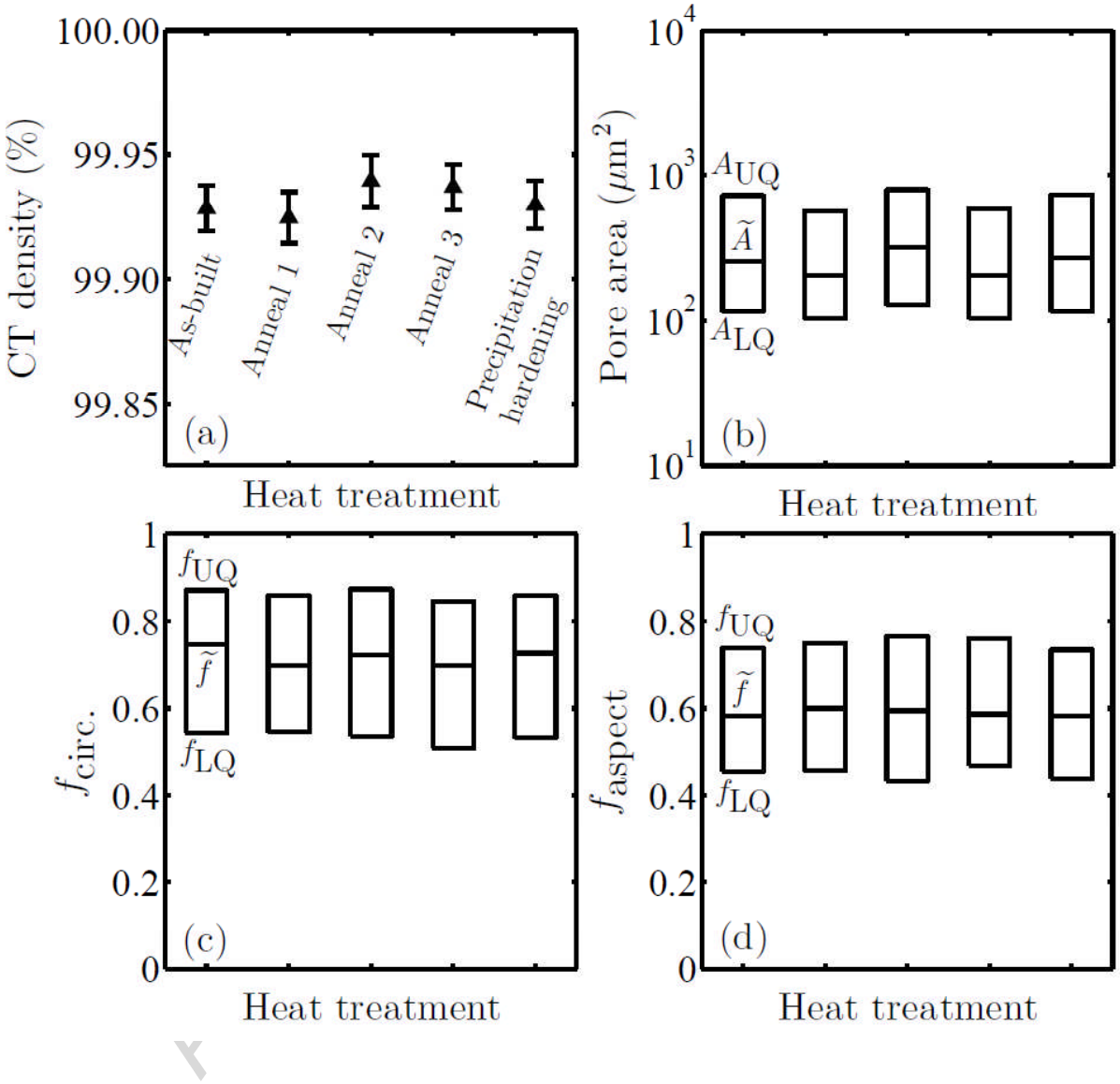


Fig. 9

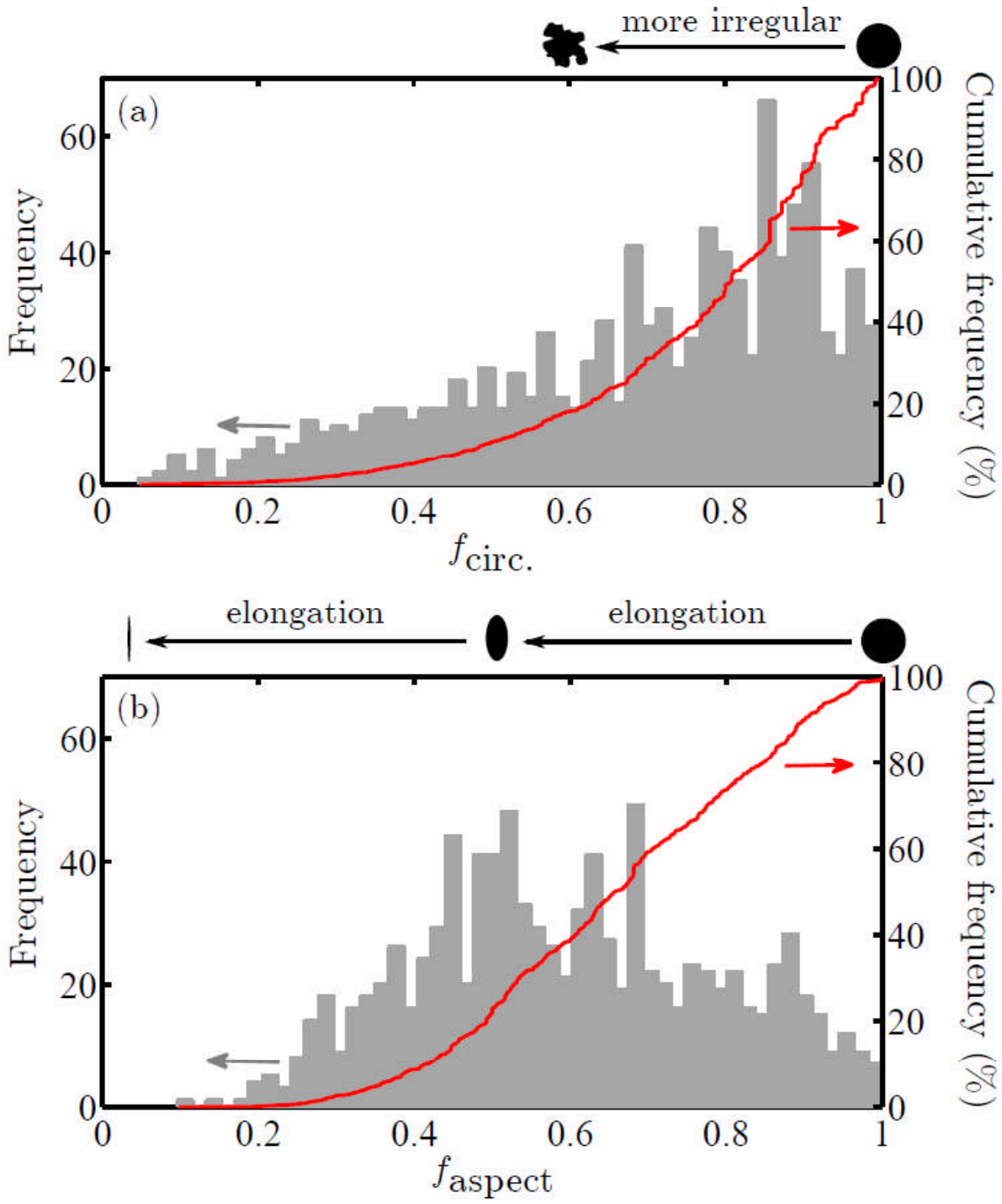


Fig. 10

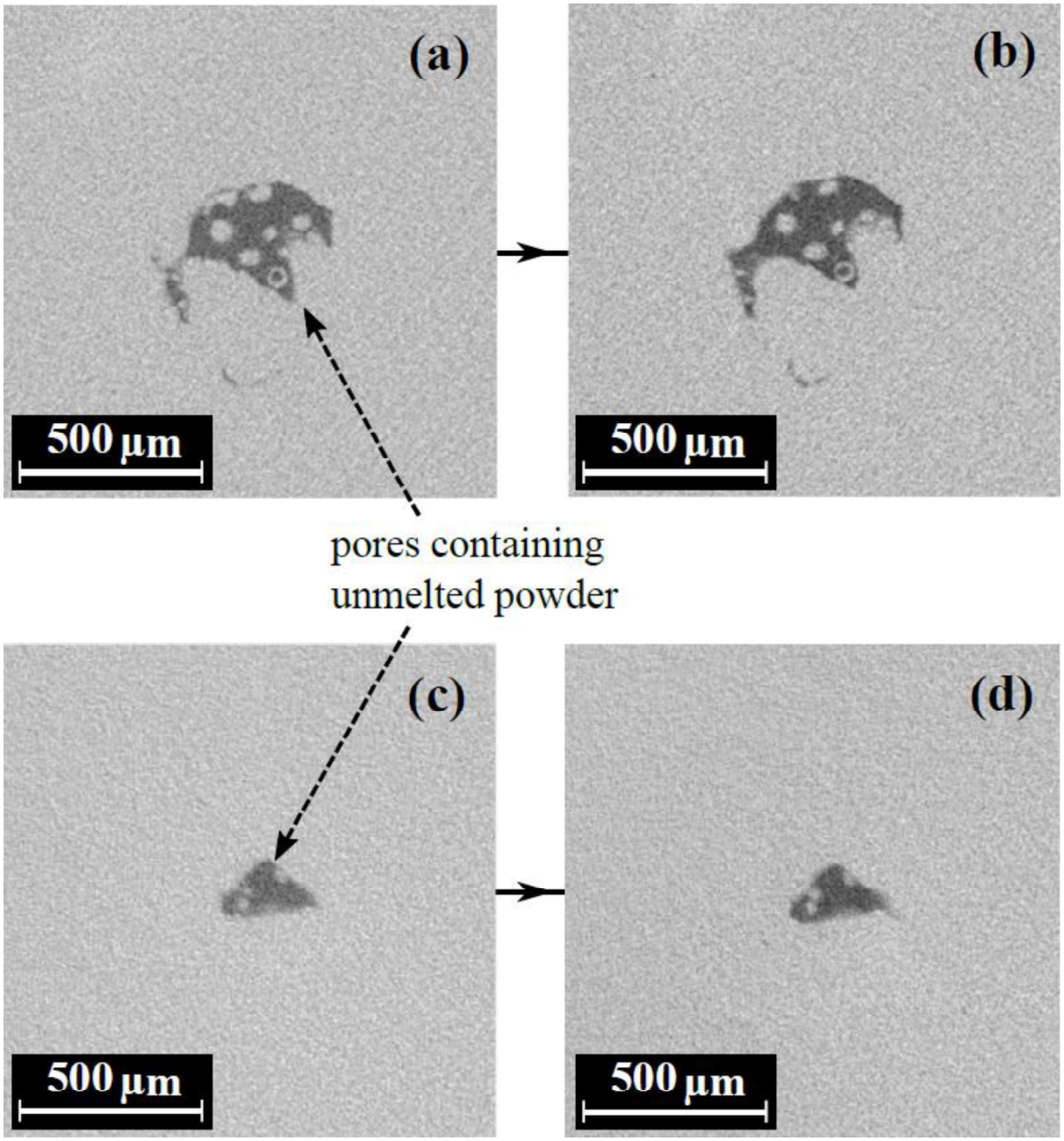


Fig. 11

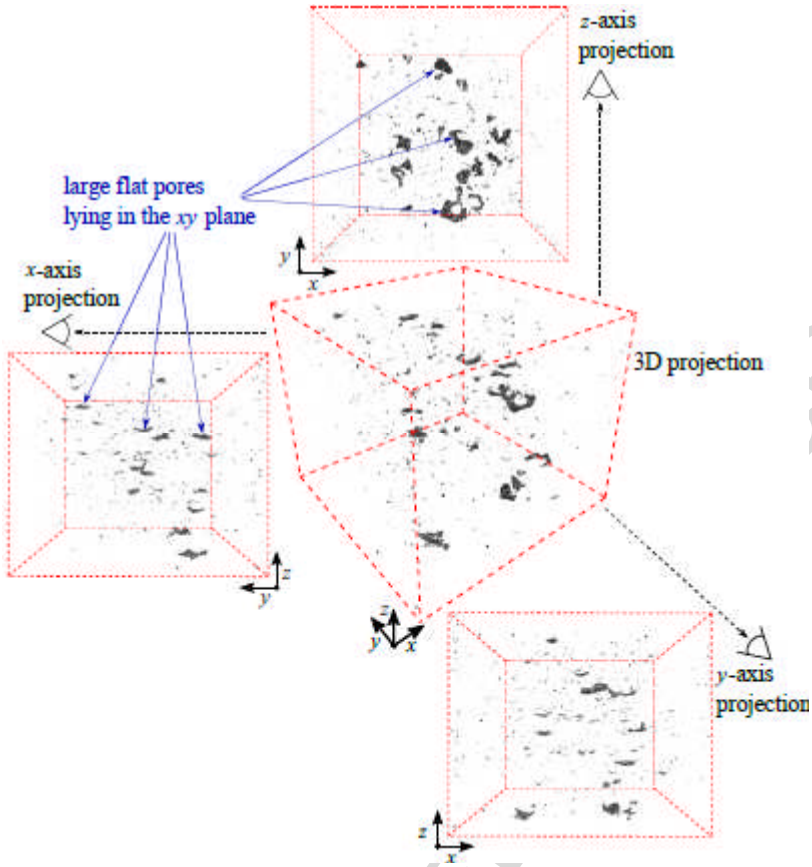


Fig.12

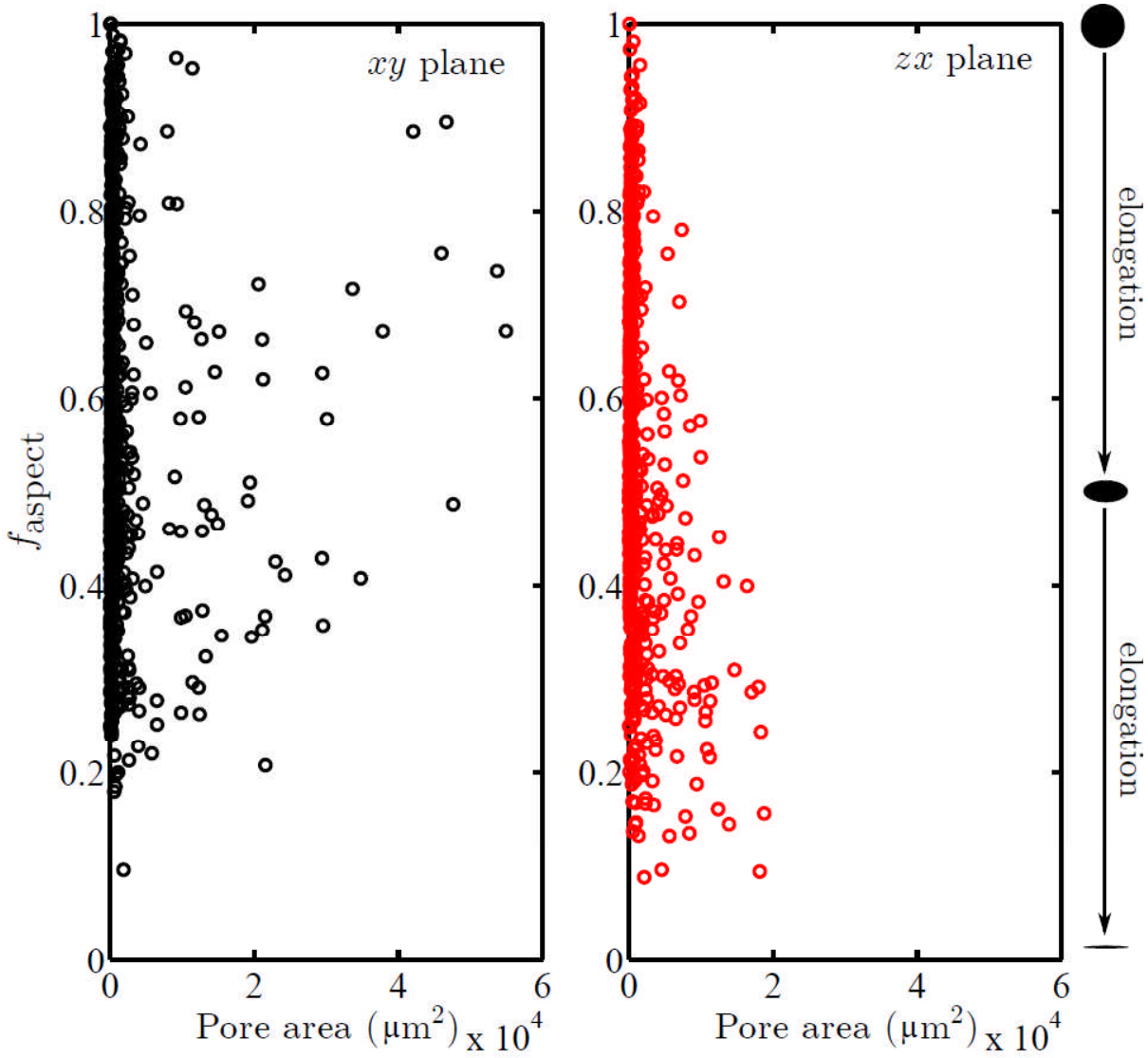


Fig. 13

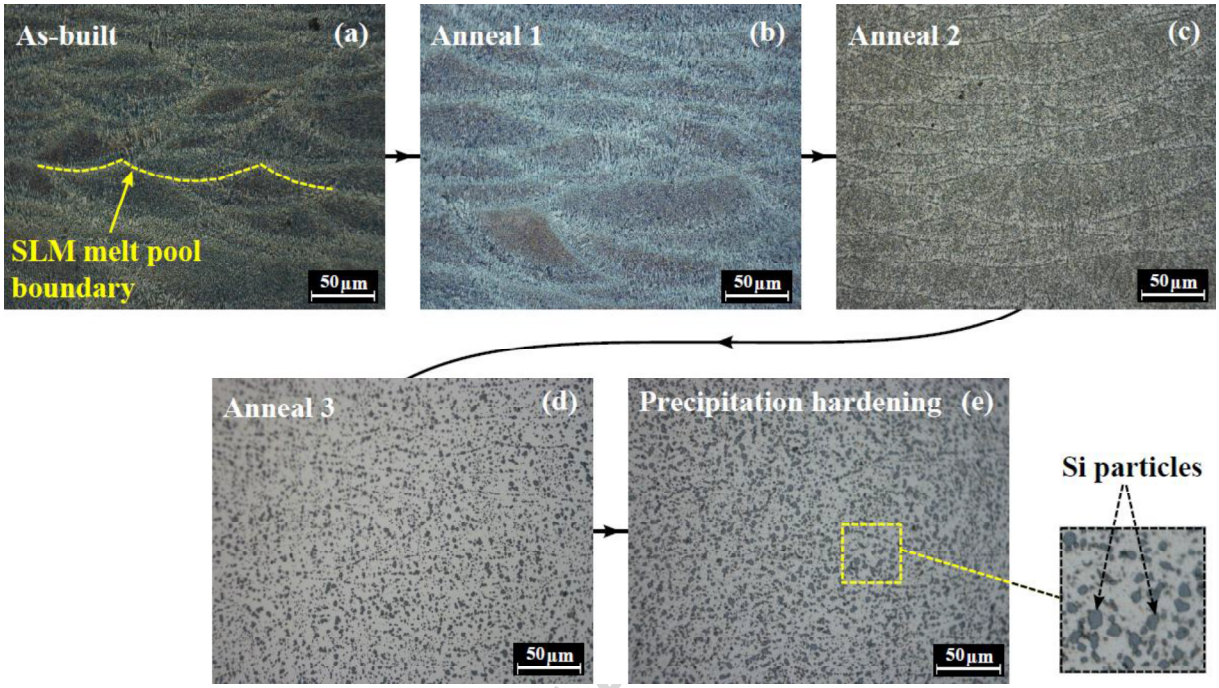


Fig. 14

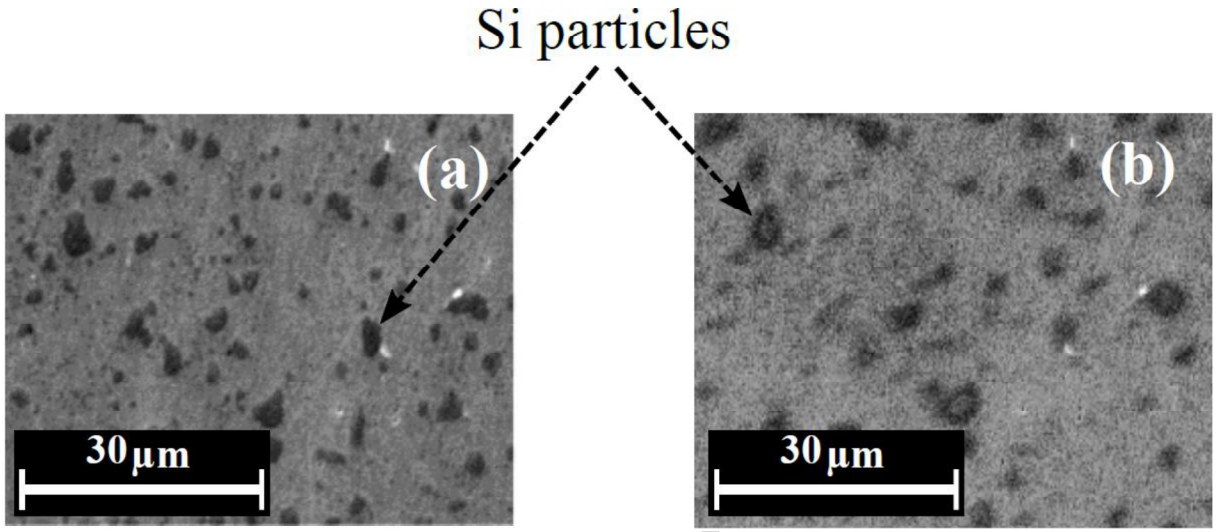


Fig. `15

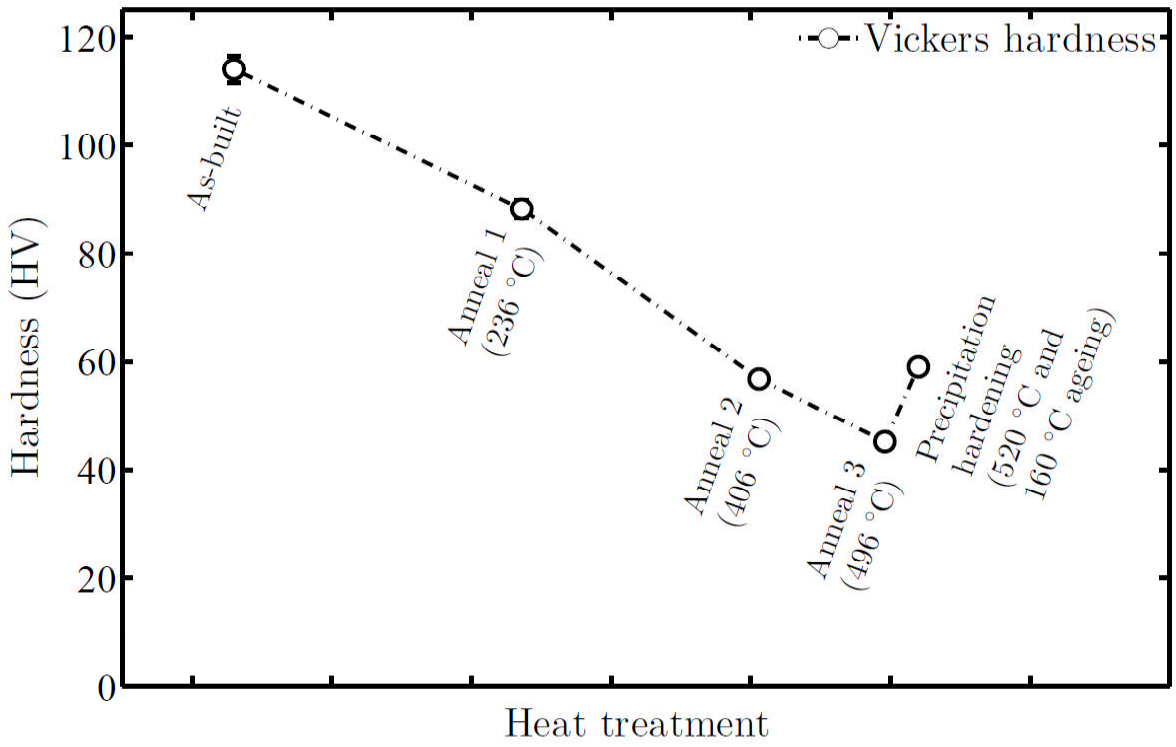


Fig. 16

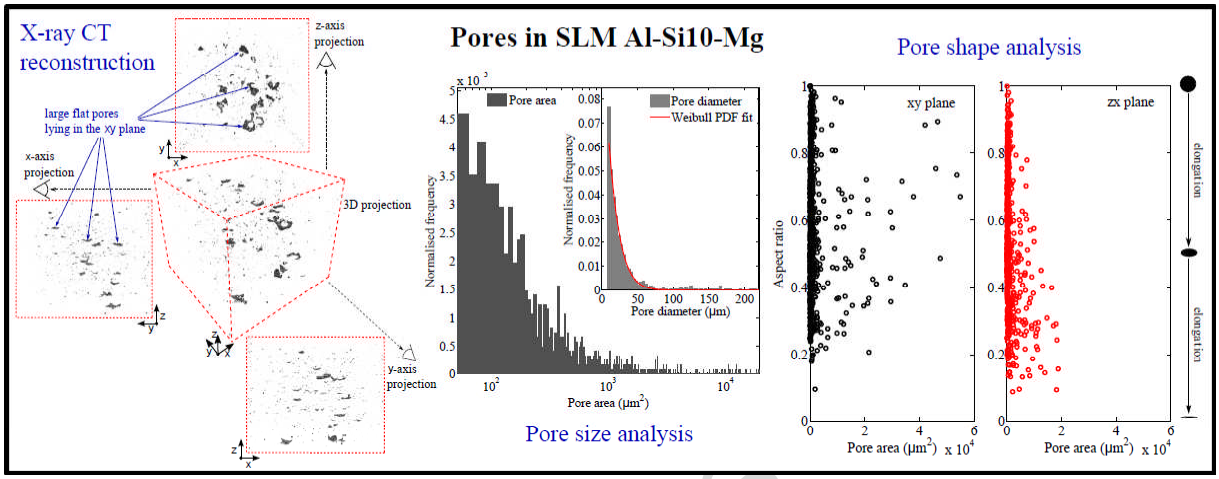


Graphical abstract